The Astrophysical Journal, 723:530–543, 2010 November 1 doi:10.1088/0004-637X/723/1/530

STAR FORMATION AND DUST OBSCURATION IN THE TIDALLY DISTORTED GALAXY NGC 2442

Anna Pancoast[1,2], Anna Sajina[1], Mark Lacy[3], Alberto Noriega-Crespo[4], and Jeonghee Rho[5]
[1] Haverford College, Haverford, PA 19041, USA
[2] UC Santa Barbara, Santa Barbara, CA 93106, USA
[3] North American ALMA Science Center, National Radio Astronomy Observatory, Charlottesville, VA 22903, USA
[4] Spitzer Science Center, Caltech, Pasadena, CA 91125, USA
[5] NASA Ames Research Center, SOFIA, M/C 211-3, Moffett Field, CA 94035, USA
Received 2010 April 27; accepted 2010 August 17; published 2010 October 12

ABSTRACT

We present a detailed investigation of the morphological distribution and level of star formation and dust obscuration in the nearby tidally distorted galaxy NGC 2442. *Spitzer* images in the IR at 3.6, 4.5, 5.8, 8.0, and 24 μm and *GALEX* images at 1500 Å and 2300 Å allow us to resolve the galaxy on scales between ∼240 and 600 pc. We supplement these with archival data in the *B*, *J*, *H*, and *K* bands. We use the 8 μm, 24 μm, and FUV (1500 Å) emission to study the star formation rate (SFR). We find that, globally, these tracers of star formation give a range of results of ∼6–11 $M_{\odot}$ yr^{-1}, with the dust-corrected FUV giving the highest value of SFR. We can reconcile the UV- and IR-based estimates by adopting a steeper UV extinction curve that lies in between the starburst (Calzetti) and Small Magellanic Cloud extinction curves. However, the regions of the highest SFR intensity along the spiral arms are consistent with a starburst-like extinction. Overall, the level of star formation we find is higher than previously published for this galaxy, by about a factor of 2, which, contrary to previous conclusions, implies that the interaction that caused the distorted morphology of NGC 2442 likely also triggered increased levels of star formation activity. We also find marked asymmetry in that the north spiral arm has a noticeably higher SFR than the southern arm. The tip of the southern spiral arm shows a likely tidally distorted peculiar morphology. It is UV bright and shows unusual IRAC colors, consistent with other published tidal features IRAC data. Outside of the spiral arms, we discover what appears to be a superbubble, ∼1.7 kpc across, which is seen most clearly in the IRAC images. Significant Hα, UV, and IR emission in the area also suggest vigorous ongoing star formation. A known, recent supernova (SN 1999ga) is located at the edge of this superbubble. Although speculative at this stage, this area suggests a large star-forming region with a morphology shaped by generations of supernovae. Lastly, we discover an 8 μm (polycyclic aromatic hydrocarbon) circumnuclear ring with an ∼0.8 kpc radius. The Hα emission is largely concentrated inside that ring and shows a vague spiral structure in the rest of the galaxy. The nuclear region shows the highest obscuration levels in the galaxy (A_{1600} ∼ 3–4) most likely due to the circumnuclear dust ring.

Key words: galaxies: individual (NGC 2442) – galaxies: star formation – galaxies: structure

Online-only material: color figures

1. INTRODUCTION

One of the most important quantities we derive for both individual galaxies and for populations used in studies of galaxy evolution is the star formation rate (SFR). Historically, we have relied on two principle diagnostics: the UV emission of young stars and the IR emission of starlight-heated dust. The principal drawback of the UV approach is the strong extinction dependence, which can be somewhat corrected, for example, by using the UV slope (Calzetti et al. 1994; Meurer et al. 1999; Kong et al. 2004). This relation is different for non-starbursting versus starbursting galaxies potentially due to the influence of older stellar populations (Cortese et al. 2006; Dale et al. 2007), as well as differences in extinction laws (Boquien et al. 2009b). The relation often fails for IR-selected starbursts (Buat et al. 2005), including submillimeter galaxies (SMGs) and dusty red galaxies (DRGs; see, e.g., Reddy et al. 2006). The IR approach's principle drawback is spectral energy distribution (SED) variations which can affect bolometric versus monochromatic estimates, as well as dust heating by older stellar populations. This is believed to be especially significant for polycyclic aromatic hydrocarbon (PAH) emission (e.g., broadband 8 μm) and long wavelength cold dust emission, but less of an issue for the warm dust dominating the mid-IR continuum (e.g., broadband 24 μm; Peeters et al. 2002; Calzetti et al. 2005). IR-based relations may also underestimate the SFR if a significant fraction of the starlight is unobscured by dust, although this is partially mitigated by the conversion factors. More fundamentally, the conversion relations we use are ultimately calibrated on stellar population synthesis models and nearby populations of both normal and starburst galaxies (see Kennicutt 1998) typically using total galaxy values. This effectively averages highly obscured with unobscured regions and could lead to underestimating the dust content in high redshift interacting galaxies (Charmandaris et al. 2004). In order to further understand the limitations of these estimates, we would like to see how well these relations hold up on smaller galactic scales, as was done in the case of M51 by Calzetti et al. (2005).

By $z \sim 1$, the SFR density is believed to be dominated by luminous infrared galaxies or LIRGs (Le Floc'h et al. 2005). Recent work suggests that in such galaxies star formation activity is likely to be largely triggered by mergers and tidal interactions (Bridge et al. 2007; Shi et al. 2009). Therefore, we are particularly interested to test how different SFR tracers and broadband obscuration diagnostics behave in galaxies undergoing such interactions. Moreover, an investigation of the localized SFR in such galaxies can give us insight into the details of how interactions trigger star formation.

The nearby peculiar spiral galaxy NGC 2442 provides such an opportunity. It appears tidally distorted with areas of high SFR in the asymmetric spiral arms and nuclear region. The tidal distortion is thought to be the result of either ram pressure stripping from interaction with an inhomogeneous intergalactic medium (IGM; Ryder et al. 2001) or a tidal interaction with a neighboring galaxy (Mihos & Bothun 1997). At a distance of 20.7 Mpc ($z = 0.004890$, NED[6]), NGC 2442 is significantly closer to us than, for example, the bulk of the members of the Arp Atlas of peculiar galaxies (Arp 1966).[7] Some interesting observations include: a low-ionization nuclear emission-line region (LINER) nucleus (Bajaja et al. 1999), an anomalous magnetic region somewhat offset from the bulk of the galaxy (Harnett et al. 2004), a recent supernova, SN 1999ga (Woodings et al. 1999; Pastorello et al. 2009), and lastly a massive dark H I cloud just beyond the northern spiral arm (Ryder et al. 2001).

In this paper, we use a multi-wavelength data set to identify and compare areas of high SFR and dust obscuration in NGC 2442. We identify regions of high SFR using emission in the UV and infrared: spectral regions that trace the original and reprocessed UV light from young, hot stars, respectively (for a review of star formation tracers see Kennicutt 1998). The *Galaxy Evolution Explorer* (*GALEX*; Martin et al. 2005) and *Spitzer Space Telescope* (Werner et al. 2004) allow for high sensitivity observations of NGC 2442 in the UV and IR. Throughout this paper, we assume a flat Λ-dominated universe with $H_o = 71\,\mathrm{km\,s^{-1}\,Mpc^{-1}}$, $\Omega_\mathrm{M} = 0.27$, and $\Omega_\Lambda = 0.73$ (Spergel et al. 2003). At the redshift of NGC 2442, this implies $1'' \sim 100$ pc.

2. DATA

2.1. Spitzer Mid-IR Images

NGC 2442 was observed at 3.6, 4.5, 5.8, and 8.0 μm with the *Spitzer* Infrared Array Camera (IRAC; Fazio et al. 2004) and at 24 μm with the Multiband Imaging Photometer for *Spitzer* (MIPS; Rieke et al. 2004) as part of the *Spitzer* science verification observations. The IRAC images were taken on 2003 November 21. The MIPS data were also obtained early in the mission to cross-check the performance of the 70 μm array in all observing modes, including Scan Mapping, that takes data on the three MIPS bands (24, 70, and 160 μm). The scan data were taken at a slow scan rate (10 s per pointing) over a half-degree leg (FOV $\sim 5' \times 30'$), with a total integration time of 50 s at 24 μm. In this paper, we mostly focus on the 24 μm data due to its higher resolution; however, we refer to the 70 μm and 160 μm data as well when discussing the total SFR. The IRAC images ideally resolve the galaxy on scales of 1.″0, 1.″1, 1.″4, and 2.″0 for the 3.6 μm through 8.0 μm images, respectively. However, the effective resolution of IRAC channels 1 and 2 is limited to 1.″2 due to the detector pixelization.

The 24 μm image has a resolution of 5.″8. All *Spitzer* images are in units of MJy/sr, after all the standard pipeline processing. For our analysis, we convert all other images (see below) to the same units. We also perform a background subtraction for each image by subtracting the mean of the background in a large patch near the galaxy (the mean and median were essentially the same). The 5.8 μm image has a patchy background (due to varying dark levels in the detector as a function of time—the "first frame" effect), but for a bright galaxy like ours and given that the 5.8 μm band is not crucial in our analysis, we did not consider it necessary to clean this image further. For this image, we used the average value from multiple patches to perform a background subtraction.

2.2. Optical/Near-IR Images

An optical *B*-band (0.44 μm) image of NGC 2442 was taken using the Cerro Tololo Inter-American Observatory (CTIO) as part of the Bright Spiral Galaxy Survey (Eskridge et al. 2002) and was available through the NASA/IPAC Extragalactic Database (NED). The *B*-band image has a resolution of 1.″5 and was first background subtracted and then flux calibrated using the value for the total galaxy flux given in Sersic & Donzelli (1993). This is a very rough "calibration," but as we only make very limited use of this image, we felt it was sufficient.

Near-IR images of NGC 2442 in the *J*, *H*, and *K* bands (1.2, 1.65, and 2.2 μm) were obtained as part of the Two Micron All Sky Survey (2MASS; Skrutskie et al. 2006) and available, already background subtracted, through NED (for details see Jarrett et al. 2003). We converted the units of these images from pixel counts to MJy/sr by relating flux to pixel counts by

$$\frac{F[\mathrm{Jy}]}{\mathrm{pixel}} = F_o * 10^{-0.4(\mathrm{MAGZP}-2.5\log(\mathrm{S}))}, \quad (1)$$

where MAGZP is given in the FITS header for each image, and $F_o[\mathrm{J}] = 1594$ Jy, $F_o[\mathrm{H}] = 1024$ Jy, and $F_o[\mathrm{K}] = 666.8$ Jy, as given by Cohen et al. (2003). The 2MASS images have a resolution of 2.″5.

2.3. UV Images

GALEX images of NGC 2442 were taken in the far-ultraviolet around 1500 Å (FUV, 1350–1750 Å) and in the near-ultraviolet around 2300 Å (NUV, 1750–2750 Å) as part of targeted observations (PI: Mark Lacy). The NUV image was taken on 2005 March 24 with an exposure time of 2.64 hr and the FUV image was taken on 2006 January 24 with an exposure time of 1.54 hr. These images were included in the UV Atlas of Nearby Galaxies by Gil de Paz et al. (2007). The *GALEX* images have resolutions of 4.″2 for the FUV and 5.″3 for the NUV (Morrissey et al. 2007). We converted the units of these images from counts per second (cps) to MJy/sr using $F[\mathrm{MJy/sr}] = 0.638 * F_\mathrm{NUV}[\mathrm{cps}]/\mathrm{pixel}$ and $F[\mathrm{MJy/sr}] = 2.036 * F_\mathrm{FUV}[\mathrm{cps}]/\mathrm{pixel}$ which are derived from

$$m_\mathrm{AB} = -2.5 * \log\left(\frac{\mathrm{cps}}{rr}\right) + m_{\mathrm{o,AB}}, \quad (2)$$

where $rr \sim 1$, $m_{\mathrm{o,AB}}[\mathrm{NUV}] = 20.08$, and $m_{\mathrm{o,AB}}[\mathrm{FUV}] = 18.82$ (see the *GALEX* Observer's Guide). We background subtract both images and check that the final total fluxes for the galaxy are very close to those calculated by Gil de Paz et al. (2007).

2.4. Foreground Extinction Correction

This galaxy has a significant foreground extinction, which strongly affects the observed UV emission, but also affects the *B*, *J*, *H*, and *K* bands while, by extrapolation, it is likely negligible in the IRAC bands. We adopt the following values for the UV foreground: $A_\mathrm{FUV} = 1.60$ and $A_\mathrm{NUV} = 1.62$ (Gil de Paz et al. 2007). The optical/near-IR Milky Way (MW) extinction values,

[6] NASA/IPAC Extragalactic Database.

[7] While the original atlas does not include distance estimates, Smith et al. (2007) have selected a subset of the Arp galaxies which have angular sizes $>3'$ and hence are biased to the more nearby members of the Arp catalog. This sub-sample has luminosity distances in the range ~6–150 Mpc, with only two galaxies having smaller distances than NGC 2442.

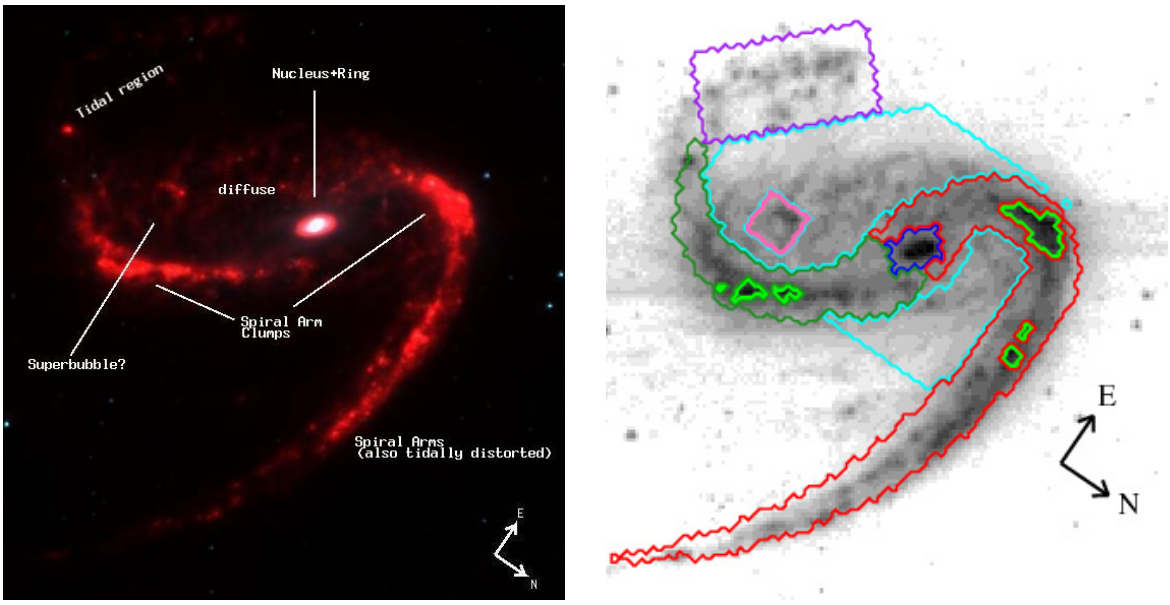

Figure 1. Left: the 8 μm IRAC image of NGC 2442 where we label the key regions of interest. Right: a $7' \times 7'$ cutout of the 8 μm image of NGC 2442. The colored contours show the masks applied in this paper to select regions of interest, where red shows the north spiral arm mask, dark green shows the south spiral arm, green shows the spiral clumps mask, cyan shows the diffuse region mask, pink shows the superbubble mask, dark blue shows the nuclear region, and magenta shows the southern tidal region mask. Note that the nuclear region mask includes both the nucleus and nuclear ring (see the left panel).

taken from NED, are $A_B = 0.874, A_J = 0.183, A_H = 0.117$, and $A_K = 0.074$. These corrections are applied to all UV-to-near-IR images prior to any subsequent analysis.

3. ANALYSIS

3.1. Image Alignment

To facilitate the multi-wavelength analysis presented in this paper, the above images were aligned and rebinned to a common pixel scale. This procedure was carried out using the IDL FREBIN function, which conserves flux. The pixel scale was chosen to be at least as large as the resolution of the poorest resolution image. For analysis that only uses IRAC and 2MASS images, we adopt a pixel scale of 2.″4, and for the rest we adopt a pixel scale of 6.″0. The first pixel scale corresponds to 240 pc and the second to 600 pc at the redshift of NGC 2442.

3.2. Isolating Regions of Interest

In order to compare star formation and dust obscuration in different areas of NGC 2442, we generate masks that isolate prominent physical features of the galaxy as shown in Figure 1.

1. *North and south spiral arms.* These are defined as shown in Figure 1. Previous work by Mihos & Bothun (1997), based on Hα observations, showed that the northern spiral arm is likely stronger in terms of star formation compared with the southern arm and hence we also include this north–south distinction. Note that the tip of the southern arm is treated separately in the "Tidal region" below.
2. *Star-forming clumps/knots.* These are areas inside the spiral arms that are particularly bright at 24 μm (presumably due to intense star formation). We define the masks by setting a threshold of 24 μm pixel value of >7.5 MJy sr^{-1} which corresponds to an SFR intensity of 0.062 $M_\odot$ yr^{-1} kpc^{-2}.
3. *Nuclear region.* This region can be resolved into a nucleus and a circumnuclear ring in the IRAC images (see Figure 1), which was also suggested by Mihos & Bothun (1997) on the basis of their Hα map of the galaxy. The radius of this circumnuclear ring is $\sim$0.8 kpc. It is most prominent in the IRAC 8 μm image, suggesting it is a strong PAH emitter. As mentioned in the introduction, the nucleus of NGC 2442 has a LINER spectrum (Bajaja et al. 1999). Note that, apart from its treatment in the body of this paper alongside the rest of the regions of interest, we include an Appendix where we discuss the observed properties of the nuclear region in further detail.
4. *Diffuse.* This includes the filamentary structure outside the spiral arms in the IRAC images, especially prominent on the southern side of the galaxy (see Figure 1). This region is also a strong UV emitter.
5. *Tidal region.* This may simply be an extension of the southern arm, but due to its disturbed morphology, suggestive of tidal debris, we treat it separately.
6. *Superbubble.* This is a spherical-looking area within the diffuse region, to the southwest of the nuclear region, with a diameter of $\sim$1.7 kpc. SN 1999ga (Woodings et al. 1999; Pastorello et al. 2009) is found on the edge of this structure.

Similar studies of resolved galaxies have also used multi-pixel apertures placed specifically over regions of interest (see Calzetti et al. 2005; Smith et al. 2007; Boquien et al. 2009a; Zhang et al. 2010). Our approach means that essentially all of the galaxy falls inside one of our masks, and therefore we can truly investigate, for example, which region dominates which part of the total SED. The total galaxy aperture covers 1063 kpc^2 and includes all the regions of interest. Table 1 lists the different masks (including the total galaxy mask) in order of decreasing area covered. We also list the total luminosities in each region in the FUV, 8 μm, and 24 μm bands.

4. RESULTS

4.1. Spectral Energy Distribution and Mid-IR Colors

Figure 2 shows the UV-to-IR SED of NGC 2442. For comparison, we overlay an Sc spiral galaxy template (Polletta

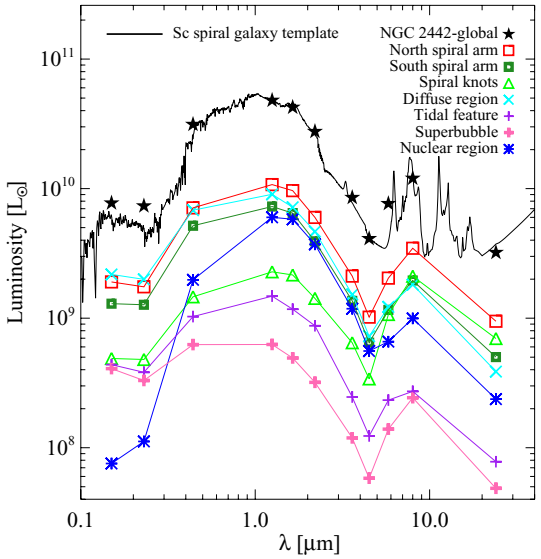

Figure 2. SED of NGC 2442 showing the total luminosity in each band for the whole galaxy as well as individually for each region of interest. Template of an Sc spiral galaxy template from SWIRE library overlaid for comparison (Polletta et al. 2007).

(A color version of this figure is available in the online journal.)

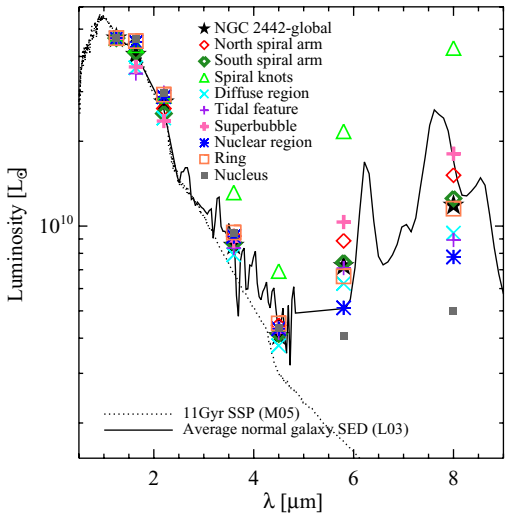

Figure 3. Detailed near-IR SED of the total galaxy and regions of interest normalized to the *J* band. An 11 Gyr old SSP model (M05; Maraston 2005), and a normal galaxies average spectrum (L03; Lu et al. 2003) are overplotted for comparison.

(A color version of this figure is available in the online journal.)

Table 1
Mask Region and Total Galaxy Luminosity Data

Region[a]	Pixels	log(L(FUV)) ($L_\odot$)	log(L(8)) ($L_\odot$)	log(L(24)) ($L_\odot$)
Total galaxy	2952	9.92	10.08	9.51
Diffuse region	461	9.35	9.26	8.59
North spiral arm	354	9.28	9.54	8.98
Tidal feature	189.0	8.68	8.43	7.89
South spiral arm	166	9.11	9.29	8.70
Spiral knots	37	8.69	9.32	8.84
Superbubble	25.0	8.61	8.39	7.69
Nuclear region	22.0	7.88	9.00	8.38

Note. [a] The aperture used for the total galaxy covers 1063 kpc^2, corresponding to 2952 pixels of dimension $6'' \times 6'' = 0.6$ kpc $\times$ 0.6 kpc.

et al. 2007), which is a good match to NGC 2442 in the near-IR to mid-IR, but is somewhat under-luminous in the UV. Figure 2 also shows the SED of each region of interest. The SEDs of the northern and southern spiral arms are very similar although the northern arm is more luminous. Apart from those two masks, we find that, as expected, there is significant variation in the SED shape across the galaxy. The IR emission (at 24 μm) appears strongly concentrated along the spiral arms (including the north and south spiral arms and the spiral knots). By contrast, the UV emission is much more spread out with the strongest emission coming from the diffuse region. We will return to this point in Section 4.4. The nuclear region is extremely UV poor and moreover has the reddest UV color suggesting high levels of obscuration (see Section 4.3). Relative to the rest of their SEDs, the strongest UV emitters are the tidal region at the tip of the southern spiral arm and even more extremely the superbubble region. We discuss possible interpretations of the origin of the superbubble region in Section 4.2.

To investigate more closely the relative strength of the PAH emission features that are believed to dominate the broadband 5.8 μm and 8.0 μm fluxes, Figure 3 shows a more detailed view of the near-IR SED for the total galaxy and regions of interest. The higher resolution of the *J* 8.0 μm bands allows for separation of the nuclear ring and nucleus, although the composite nuclear region is shown for comparison. The SED for each region of interest has been normalized to the *J* band, representing a stellar mass normalization. An 11 Gyr old single stellar population (SSP) model from Maraston (2005) has also been plotted. The total galaxy SED is in very good agreement with the *Infrared Space Observatory* (*ISO*) average spectrum of normal galaxies from Lu et al. (2003). The observed excess over the pure stellar population model at 5.8 and 8.0 μm is likely due to the 6.2 and 7.7 μm PAH emission features. Lu et al. (2003) suggest that the excess at ~4–5 μm seen in the spectra of normal galaxies is due to the presence of hot (~1000 K) dust. We find evidence of this excess in all of our regions, suggesting hot dust is present throughout this galaxy. We have tested this conclusion against a range of stellar population ages and both a burst and a nearly constant star formation (*e*-folding time of 10 Gyr). The spiral knots excess at 3.6 μm is most likely due to the 3.3 μm PAH emission feature.

Compared to the small spreads in the *H* 4.5 μm bands (a product of our *J*-band normalization and the relatively constant old stellar populations spectral shape in this regime) for the different regions of interest, the spread in the 5.8 and 8.0 μm bands is 3–4 times larger, suggesting considerable variation in the relative PAH strength in the different regions. Relative to the stellar mass, the spiral knots and the superbubble region show the strongest PAH emission. In the nuclear region, the ring is the stronger infrared emitter, while the nucleus is more dominated by the stellar emission.

Another common way to compare emission from the old stellar population, emitted in the 3.6 and 4.5 μm bands, with emission from PAH in the 5.8 and 8.0 μm bands that trace young stellar populations, is the IRAC color–color plot. Sajina et al. (2005) find that star-forming regions, old stellar populations, and active galactic nuclei (AGNs) are found in distinct locations on the plot. Regions dominated by star formation are found at high color ratios while regions dominated by old stellar populations are found at lower color ratios. AGN-dominated regions are found at higher $f_{5.8}/f_{3.6}$ for a given $f_{8.0}/f_{4.5}$, due to a hot mid-IR

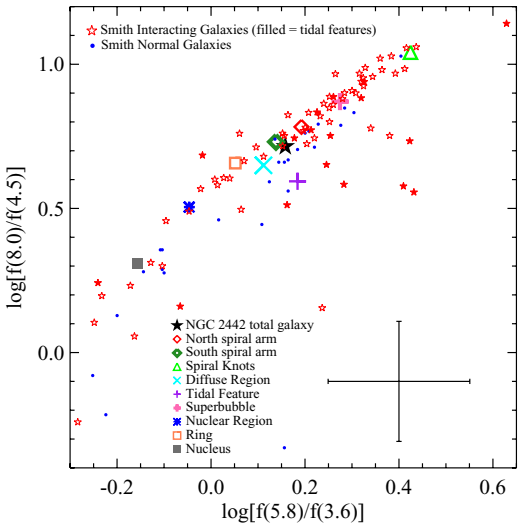

Figure 4. IRAC color–color plot showing mean values for each region of interest and Smith et al. (2007) data for normal and interacting galaxies. A representative example of the spread in pixel values for each region of interest is shown by the large error bar in the bottom right.

(A color version of this figure is available in the online journal.)

continuum. Figure 4 shows the average colors of the regions of interest. The colors are calculated using the total flux from each region of interest. However, calculating the per-pixel color and then taking the average for each region gives us an estimate of the spread in color about the mean. A representative 1σ spread in per-pixel colors for the regions of interest is shown by the large error bar. The nuclear region average data point follows the linear trend of the other average data points and does not occupy the AGN color–color space, suggesting that NGC 2442 does not have an IR AGN, despite its LINER optical spectrum (Bajaja et al. 1999). The region that deviates the most from the general trend is the tidal debris region which lies to the right of the usual PAH/stars trend. This could be due to: (1) excess hot dust, (2) varying 7.7/6.2 PAH emission ratio, or (3) a strong emission feature (s.a. molecular hydrogen) in the 5.8 μm band. Without spectra, we cannot distinguish between these possibilities.

Figure 4 also shows data from the interacting and normal galaxy samples studied by Smith et al. (2007), who also provide IRAC fluxes for the tidal features (e.g., bridges/tails) themselves. Intriguingly, we find that the colors of the tidal features from Smith et al. (2007) also tend to lie to the right of the usual relation, in agreement with our tidal region observations.

4.2. Superbubble

Figure 1 shows a bubble-shaped region outside of the spiral arms in the southern part of the galaxy (centered at R.A. = 7:36:16 and decl. = −69:33:12). The diameter of this "superbubble" is ∼1.7 kpc. Comparable sized gas superbubbles have previously been observed in starburst galaxies (e.g., Vader & Chaboyer 1995; Tsai et al. 2009) and are generally believed to be the result of hundreds of supernovae whose individual supernova remnants (SNRs) merge to form such a structure. In Figure 5, we show a comparison (over a wider region) of the ACS F658N Hα image (available from the MAST archive, PI: S. Smartt) and the IRAC 8 μm contours. The first conclusion we can draw is that there is significant Hα emission in this region (this area is also a significant UV emitter, see Figure 7). The Hα distribution in this image is not bubble-like (which is not surprising given the likely age of this structure). The Hα emission is in good agreement with our result that the superbubble region has among the highest star formation intensities in NGC 2442 (see Table 3). This area has significant radio emission (including polarized emission) as can be seen in the 6 cm radio data presented in Harnett et al. (2004). The recent supernova SN 1999ga (Pastorello et al. 2009) is located right at the edge of this superbubble. Further observations are needed to more fully understand the nature of this region; however, our current data suggest a large star-forming region outside the spiral arms, whose morphology is likely to have been shaped by generations of supernovae.

Table 2
Obscuration Values

Region	β[a]	$A_{1500,\,\mathrm{Meurer}}$ (mag)	$A_{1500,\,\mathrm{Salim}}$ (mag)	A_{1500}, IR-matched[b] (mag)
Total galaxy	−1.2	2.0	1.42	1.5
Diffuse region	−1.3	1.9	1.34	0.6
North spiral arm	−1.2	2.0	1.42	1.8
Tidal feature	−1.5	1.4	0.96	0.6
South spiral arm	−1.0	2.4	1.73	1.4
Spiral knots	−1.0	2.4	1.73	2.9
Superbubble	−1.5	1.4	0.96	0.2
Nuclear region	−0.01	4.4	3.28	3.5

Notes.
[a] The UV–slope (see Section 4.3).
[b] The UV obscuration required to match the UV and IR SFRs. Here, we adopt the $\mathrm{SFR}(24)_{\mathrm{H\,II}}$ for the IR SFR.

4.3. Dust Obscuration

The UV obscuration, A_{1500}, and the UV slope, β, defined as $f_\lambda \propto \lambda^\beta$, have been shown to be correlated, especially for starburst galaxies (Meurer et al. 1999). In terms of the *GALEX* FUV and NUV fluxes, β is derived by

$$\beta = \frac{\log(f_{\nu,1500}/f_{\nu,2300})}{\log(1500/2300)}, \quad (3)$$

where $f_{\nu,1500}$ is the specific flux at 1500 Å. To understand how the observed UV slope is related to the UV obscuration, we can re-arrange this to show that

$$\beta = \beta_o + 2.155\, A_{1500}[1 - (\kappa_{2300}/\kappa_{1500})], \quad (4)$$

where β_o is the dust-free UV slope and the ratio $\kappa_{2300}/\kappa_{1500}$ incorporates the UV slope of the extinction curve. The most widely used relation is that of Meurer et al. (1999), who find that for UV-selected starburst galaxies β and A_{1600} are related by

$$A_{1600} = 4.43 + 1.99(\beta - 2.0). \quad (5)$$

Note that this differs slightly from the form of the Meurer et al. (1999) relation because their β is defined in terms of f_λ and ours in terms of f_ν. The uncertainty in A_{1600} is 0.08 mag and in β it is 0.04. We take $A_{1600} = A_{1500}$ (since this correction is expected to be relatively negligible). We begin by assuming this relation; however, we return to the question of the most appropriate extinction curve in Section 4.5.

Based on Equation (5), the area of highest obscuration is the nuclear region with an average obscuration of 4.4 mag, while the rest of the galaxy is obscured by ∼1.4–2.4 mag. The average obscuration at 1500 Å is given in Table 2 for each region of interest.

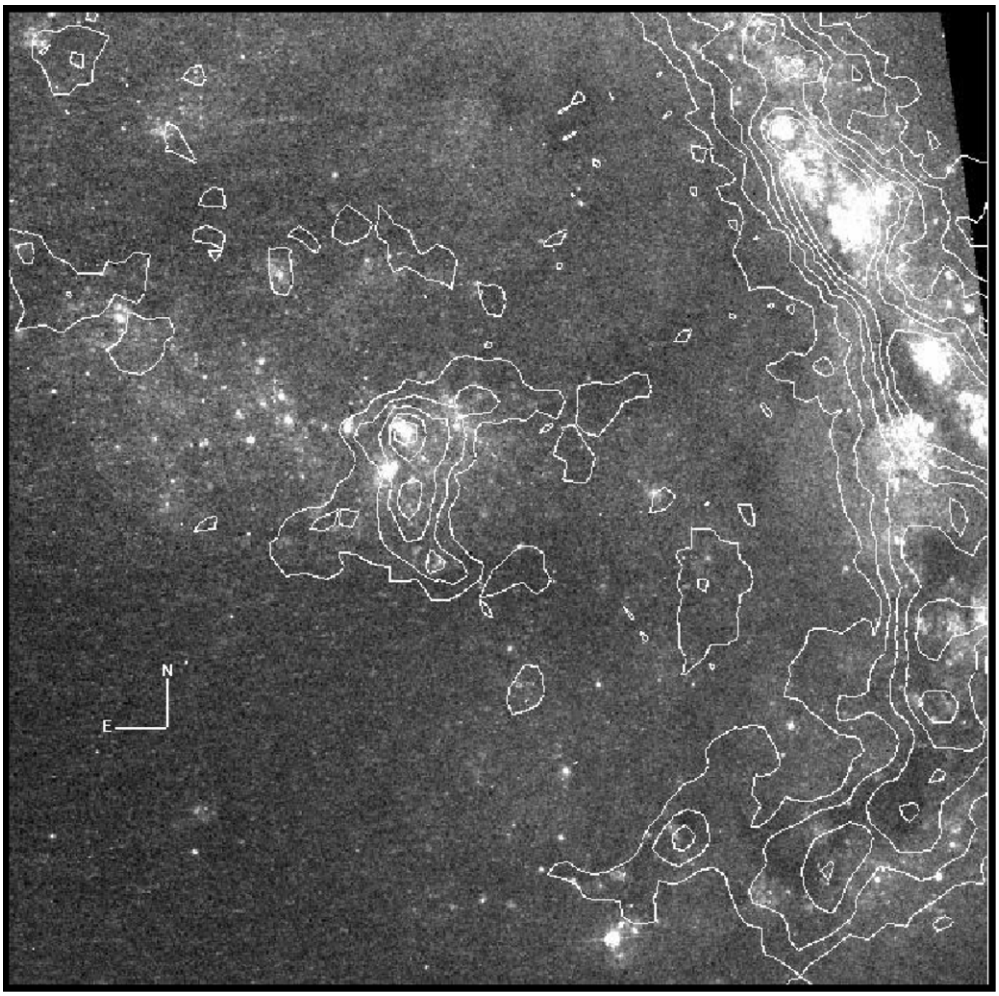

Figure 5. Gray scale shows the Hα image for part of the galaxy, whereas the contours show the IRAC 8 μm. The image is centered in the superbubble region.

The major limitation with the Meurer et al. (1999) UV–slope relation is that it is derived using starburst galaxies and shown to be a good approximation when the UV emission consists of ionizing UV photons from young stars. Calzetti et al. (2005) find that only 40% of the UV emission from the normal galaxy M51 traces current star formation, defined as populations less than 30 Myr old. This suggests that the UV–slope of normal galaxies will be affected by the older stellar population instead of only representing the preferential extinction of UV light from young stars for which it was derived.

In addition, Salim et al. (2007) calibrate relations between *GALEX* FUV and NUV bands and A_{1500} for star-forming galaxies. The relation for galaxies with (FUV–NUV) < 0.95, as found in NGC 2442, is given by

$$A_{1500} = 3.32(\mathrm{FUV}–\mathrm{NUV}) + 0.22. \quad (6)$$

We expect this relation to give a better estimate of the dust extinction in NGC 2442 than the Meurer relation as it is calibrated on normal star-forming galaxies rather than starbursts. This is discussed in more detail in Section 4.5.

4.4. Star Formation Rate

4.4.1. Comparing SFR Indicators and the SFR Maps of NGC 2442

In the literature, there is a wide array of relations to convert the FUV, 8 μm, and 24 μm luminosities to SFR. Since each SFR relation is calibrated using a different subset of galaxies or theoretical models, it is important to consider their applicability to NGC 2442. As NGC 2442 appears to be essentially an L* galaxy (see Section 4.4.2), we choose to apply SFR relations that are calibrated using normal star-forming galaxies. For greater internal consistency and to allow direct comparison with the overall SFR(Hα) presented in Section 5, we also choose infrared conversion relations that are all ultimately calibrated on the SFR(Hα) relation (Kennicutt 1998). Because we are looking at resolved star formation in NGC 2442, we consider both relations calibrated on a local and a global scale.

For a UV-based SFR, we consider both the relations in Kennicutt (1998) and in Salim et al. (2007). The latter relation gives SFR(FUV) values $\sim$30% smaller than the former. Kennicutt (1998) assumes a Salpeter (1955) initial mass function (IMF) and constant star formation. The effect of recent starbursts would paradoxically be to lower the derived SFR values (as higher UV/SFR). Salim et al. (2007) derive the SFRs of nearby galaxies by fitting their UV+optical SEDs and averaging their star formation over the past 100 Myr. These are used to calibrate a conversion relation between L_{FUV} and SFR. This relation generally results in SFRs that are $\sim$30% lower than those based on Kennicutt (1998) when it is converted from a Chabrier (Chabrier 2003) to Salpeter IMF. This is due, in part, to a departure from a constant star formation model which, as discussed above, tends to result in a lower SFR. The difference between these two relations is within the large systematic

Table 3
SFR Estimates

Region	SFR(FUV) ($M_\odot$ yr^{-1})	SFR(FUV)-corr[a] ($M_\odot$ yr^{-1})	SFR(8) ($M_\odot$ yr^{-1})	SFR(24)$_{\rm global}$[b] ($M_\odot$ yr^{-1})	SFR(24)$_{\rm H\,II}$ ($M_\odot$ yr^{-1})	SFR(FUV + 24) ($M_\odot$ yr^{-1})	SFR(FUV + 24) Intensity ($M_\odot$ yr^{-1} kpc^{-2})
Total galaxy	1.7 ± 1.2	$10.9 \pm 2.8 \pm 3.8$	7.6 ± 1.9	4.7 ± 3.4	7.4 ± 3.4	5.9	0.006
Diffuse region	0.5 ± 0.3	$2.7 \pm 0.7 \pm 0.9$	1.2 ± 0.1	0.7 ± 0.5	1.1 ± 0.5	1.0	0.006
North spiral arm	0.4 ± 0.3	$2.5 \pm 0.7 \pm 0.9$	2.2 ± 0.5	1.4 ± 1.0	2.1 ± 1.0	1.6	0.013
Tidal feature	0.10 ± 0.07	$0.4 \pm 0.1 \pm 0.1$	0.17 ± 0.02	0.15 ± 0.12	0.3 ± 0.12	0.2	0.003
South spiral arm	0.3 ± 0.2	$2.4 \pm 0.6 \pm 0.8$	1.2 ± 0.3	0.8 ± 0.6	1.1 ± 0.5	0.9	0.016
Spiral knots	0.10 ± 0.07	$0.9 \pm 0.2 \pm 0.3$	1.3 ± 0.8	0.8 ± 0.6	1.2 ± 0.6	1.0	0.076
Superbubble	0.09 ± 0.06	$0.3 \pm 0.1 \pm 0.1$	0.15 ± 0.03	0.08 ± 0.06	0.12 ± 0.06	0.2	0.017
Nuclear region	0.02 ± 0.01	$0.9 \pm 0.2 \pm 0.3$	0.6 ± 0.4	0.3 ± 0.2	0.4 ± 0.2	0.3	0.041

Notes.
[a] SFR(FUV)-corr is corrected for dust obscuration by multiplying the uncorrected SFR by $e^{A_{1600}/1.086}$. The uncertainty in SFR(FUV) is from the spread in SFR(FUV) relations in the literature, while the uncertainty in SFR(FUV)-corr is from the uncertainty in the UV–slope dust correction (the first number) and the spread in the SFR(FUV) relations (the second number).
[b] SFR(24)$_{\rm global}$ is calculated using a nonlinear relation calibrated using integrated normal star-forming galaxies by Zhu et al. (2008) and given in Calzetti et al. (2010), while SFR(24)$_{\rm H\,II}$ is calculated using a nonlinear relation calibrated using H II regions by Relaño et al. (2007).

uncertainty quoted in Kennicutt (1998); however, since NGC 2442 has a tidally distorted morphology and regions of higher SFR intensity (as is discussed later in this section), it is more likely that there were recent bursts rather than a constant star formation history over the past $\lesssim$100 Myr. Therefore, we adopt the Salim et al. (2007) relation. We adopt a 0.15 dex 1σ systematic uncertainty on SFR(FUV) (see Kennicutt 1998; Salim et al. 2007).

We derive SFR(8) and SFR(24)$_{\rm global}$ based on the relations presented in Zhu et al. (2008). These are calibrated based on the correlation between total integrated mid-IR luminosities of normal galaxies with the extinction corrected Hα luminosities, and applying the Kennicutt (1998) Hα–SFR relation. However, because we are looking for both the global and local SFRs, we also look at SFR relations calibrated on a local scale. Specifically, we use the SFR–L_{24} relation based on individual H II regions of normal star-forming galaxies given in Relaño et al. (2007) (SFR(24)$_{\rm H\,II}$). This again is calibrated using the extinction-corrected Hα luminosities and the Kennicutt (1998) relation. We also find this to be consistent with the Calzetti et al. (2005) L_{24}–$L_{P\alpha}$ relation for H II regions in M51, if the SFR(Pα) relation from Alonso-Herrero et al. (2006) is adopted. For more discussion on different SFR indicators and their associated uncertainties, see Kennicutt (1998) and Calzetti et al. (2010). Lastly, we also use the composite relation, SFR(FUV+24), derived by Bigiel et al. (2008). Their relation aims at deriving the star formation intensity both on a global and a local scale. It is empirically derived, based on both the SFR(Hα+24) relation in Calzetti et al. (2007) and the SFR(FUV) relation in Salim et al. (2007). Below, we summarize the relations we use:

$$\mathrm{SFR_{FUV}}[M_\odot\ \mathrm{yr}^{-1}] = 2.09 \times 10^{-10}(L_{1600\,\mathrm{A}}[L_\odot]), \quad (7)$$

$$\mathrm{SFR}_{8\,\mu\mathrm{m}}[M_\odot\ \mathrm{yr}^{-1}] = 6.33 \times 10^{-10}(L_{8\,\mu\mathrm{m}}[L_\odot]), \quad (8)$$

$$\mathrm{SFR}_{24\,\mu\mathrm{m,\,global}}[M_\odot\ \mathrm{yr}^{-1}] = 1.42 \times 10^{-8}(L_{24\,\mu\mathrm{m}}[L_\odot])^{0.848}, \quad (9)$$

$$\mathrm{SFR}_{24\,\mu\mathrm{m,\,H\,II}}[M_\odot\ \mathrm{yr}^{-1}] = 3.44 \times 10^{-9}(L_{24\,\mu\mathrm{m}}[L_\odot])^{0.97}. \quad (10)$$

Figure 6 shows the SFR intensity maps based on these relations. The areas of highest SFR intensity in decreasing order are the spiral knots, the nuclear region, and the spiral arms. Our SFR and SFR intensity estimates both globally and per region are presented in Table 3. We compare the dust-corrected SFR(FUV), SFR(8), SFR(24)$_{\rm H\,II}$, and SFR(FUV+24) values for the total galaxy and regions of interest in Figure 7, where SFR(24)$_{\rm global}$ has been calculated only for the total galaxy region and plotted with the smaller symbol.

Only the north spiral arm and the spiral knots show agreement between all SFR indicators within 1σ. In particular, this suggests that the starburst-calibrated dust correction in the FUV is applicable for these regions (we return to this point in Section 4.5). A significant outlier here is the superbubble region, which we speculate is due to the presence of a very recent starburst in that region. As expected, the SFR(8) and SFR(24) show the best agreement. Although it is surprising that this good agreement (even for the total galaxy) is not for the SFR(8) and SFR(24)$_{\rm global}$ values, which are calibrated on the same sample and using the same method (Zhu et al. 2008). This may indicate that the influence of H II regions in our galaxy is somewhat stronger than average in the Zhu et al. (2008) sample. The one somewhat outlying point is for the tidal region—in the sense that it is deficient in 8 μm emission compared to its 24 μm emission relative to the average for the galaxy. We already discussed that this region has somewhat anomalous PAH ratios in Section 4.1. The tidal region and the superbubble region are the only ones where the SFR(8) and SFR(24)$_{\rm global}$ values are closer than SFR(8) and SFR(24)$_{\rm H\,II}$.

It is important to note that the error bars shown in Figure 7 for the SFR(FUV) show the uncertainty in the dust correction; as apparent in Table 3, the uncertainty in the overall SFR(FUV) relation is much larger. Correcting the FUV emission for dust extinction introduces larger uncertainties for SFR(FUV) than for SFR(8) and SFR(24) that are only surpassed by the large intrinsic spread of 0.3 dex in SFR(FUV) relations described by Kennicutt (1998). A possible systematic uncertainty comes from using a dust obscuration correction calibrated for starburst galaxies, such as the UV–slope, which would overestimate the dustiness and L(FUV) for a normal star-forming galaxy (for a discussion of this problem see Boquien et al. 2009b). For the uncertainty in SFR(8), we employ two additional SFR(8) relations, those of Calzetti et al. (2005) and Wu et al. (2005), and use half the spread in the three relations for each region of interest to define the uncertainty. We use the same method to estimate the uncertainty in SFR(24), but employing a larger

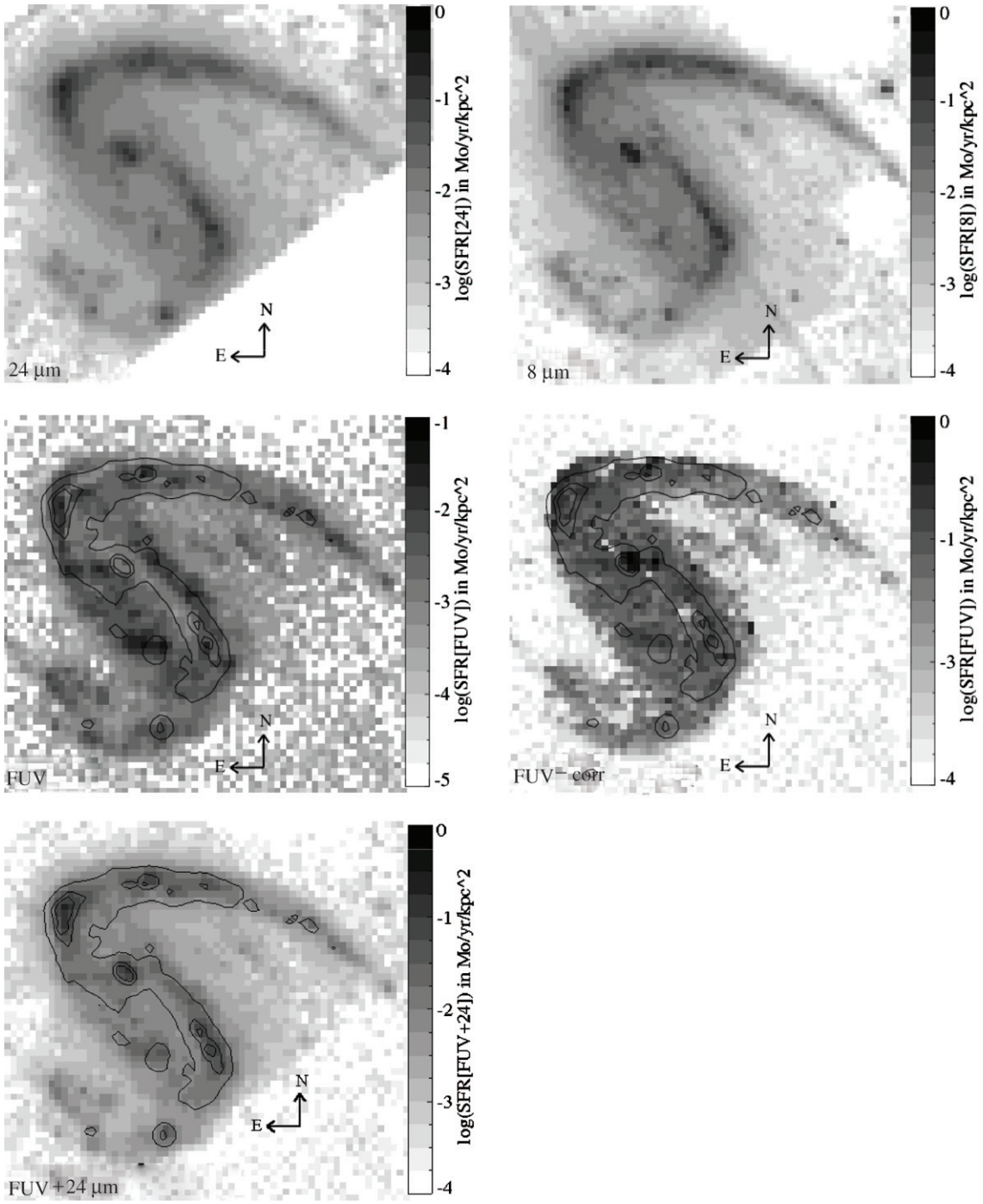

Figure 6. SFR maps from 24 μm, 8 μm, as well as dust-uncorrected and dust-corrected FUV emission and FUV+24 μm. The SFR(FUV) and SFR(FUV+24) maps have SFR(24) diagram contours overplotted at values of 0.01, 0.05, and 0.1 $M_{\odot}$ yr^{-1} kpc^{-2}. Note the different scales of SFR intensity in the case of dust-uncorrected SFR(FUV).

range of relations, including those of Alonso-Herrero et al. (2006), Calzetti et al. (2005), and Calzetti et al. (2007), a linear SFR relation given in Calzetti et al. (2010) and derived in Zhu et al. (2008),[8] and that of Rieke et al. (2009). The relations given by Alonso-Herrero et al. (2006) and Calzetti et al. (2007) are calibrated using starbursts, however, we do not find a very large discrepancy between these different SFR(24) indicators. The largest discrepancy is actually introduced by the linear relation in Zhu et al. (2008).

[8] Zhu et al. (2008) find that the data are better fit by a nonlinear model (the relation we adopt), but also derive a linear SFR relation.

4.4.2. Global SFR Indicators from Hα and Far-IR Emission

For the ease of subsequent analysis, we also derive the global SFR for NGC 2442 based on two well-established SFR indicators: Hα and the total infrared emission, $L_{\rm IR}$. The only previously published estimate of the SFR in NGC 2442 was based on its Hα emission (Mihos & Bothun 1997). Updating their value to account for the different cosmology we adopt as well as to the SFR relation in Kennicutt (1998), we find SFR(Hα) $= 4.2\,M_{\odot}$ yr^{-1} for the whole galaxy. NGC 2442 has constraints at longer wavelength (far-IR emission) based on *IRAS* observations (at 60 and 100 μm) and MIPS 160 μm

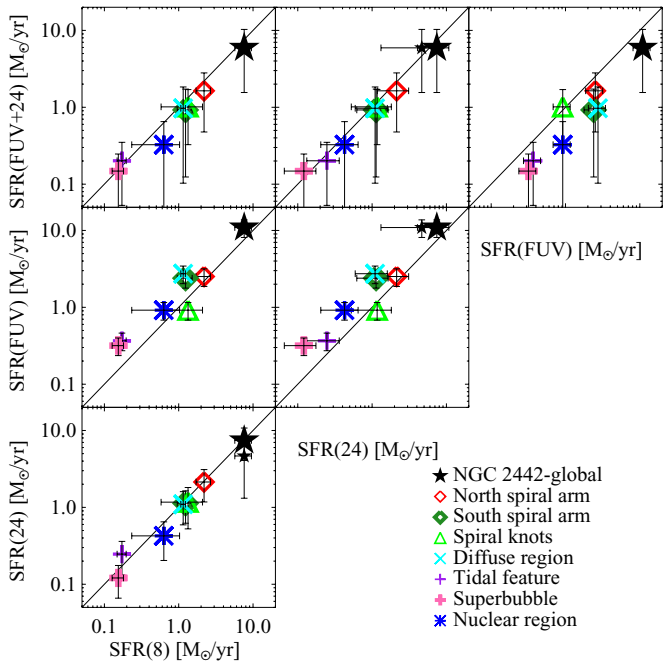

Figure 7. Comparison of SFR tracers, including SFR(24), SFR(8), and SFR(FUV), where the FUV has been corrected for dust obscuration using the UV–slope. The error bars show 1σ uncertainty. The SFR(24) used is the $\mathrm{SFR(24)_{H\,II}}$ one. $\mathrm{SFR(24)_{global}}$ is shown only for the total galaxy (the smaller black star symbol).

(A color version of this figure is available in the online journal.)

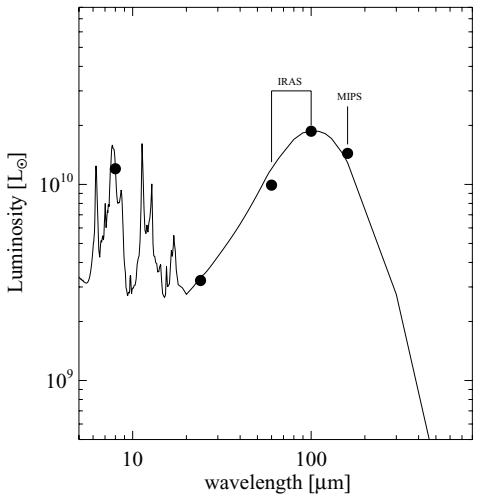

Figure 8. Global far-IR SED of NGC 2442. The SED template is the same as shown in Figure 2 (i.e., an Sc galaxy template). Along with the total galaxy 8 μm and 24 μm points as given in Table 1, we also show the IRAS 60 and 100 μm points (from NED) and the MIPS 160 μm point (we measured 57.5 Jy for the total galaxy).

observations, as shown in Figure 8. In order to accurately estimate the total $L_{\rm IR}$, we can use the constraints at longer wavelengths to choose a generic galaxy template, such as for an Sc galaxy, that fits the data and integrate the luminosity in a defined range. We calculate the integrated $L_{\rm FIR} \equiv L_{8-1000}$, giving us $\log(L_{\rm FIR}/L_\odot) = 10.53$ and $\mathrm{SFR(FIR)} = 5.85\ M_\odot \mathrm{yr}^{-1}$, based on Kennicutt (1998). Recently, Kennicutt et al. (2009) derived global composite H_α and infrared SFR relations for the SINGS galaxies, which as discussed before are similar to NGC 2442 in luminosity and hence these relations are applicable in our case. Kennicutt et al. (2009) derive relations based both on the 24 μm emission and total IR (where TIR is defined as L_{3-1000}). Based on these SINGS-calibrated relations, we obtain $\mathrm{SFR(H_\alpha{+}24)} = 6.1\ M_\odot \mathrm{yr}^{-1}$ and $\mathrm{SFR(H_\alpha{+}TIR)} = 7.1\ M_\odot \mathrm{yr}^{-1}$. These are very similar to our total galaxy SFR(FUV+24) and $\mathrm{SFR(24)_{H\,II}}$, respectively. Combined, these relations account for both direct/unobscured young stellar light, the H II regions associated with ongoing SF, and the total dust-reprocessed largely young stellar light. This leads us to believe that the true SFR is likely in the range $\sim$6–7 $M_\odot \mathrm{yr}^{-1}$.

4.5. Constraints on the Extinction Curve in NGC 2442

In the previous section, we showed that using the Meurer et al. (1999) relation to translate the observed UV slope to the UV extinction leads to larger SFRs than obtained from the IR-based relations. This is assuming the Salim et al. (2007) relation for SFR(FUV) and the discrepancy is even larger if the Kennicutt (1998) relation is used (which gives SFR(FUV) that are $\sim$30% larger). As discussed previously, the systematic uncertainty in SFR(UV) is quite significant, but for the purposes of this section it is ignored.

In Section 4.4.2, we argued that the true SFR is likely to lie in the range $\sim$6–7 $M_\odot \mathrm{yr}^{-1}$. Without dust correction, our SFR(FUV) for the total galaxy is 1.7 implying $A_{\rm FUV} = 1.4$–1.5. The Meurer et al. (1999) relation gives us $A_{\rm FUV} = 2.0$. We use the generic A_{1600} versus β relation given in Equation (4) to constrain the UV–slope of the extinction curve that would reconcile the UV- and IR-based SFR estimates. Meurer et al. (1999) already discussed that, for star-forming galaxies, the range in the dust-free UV slope, β_o, is relatively small (-2.6 to -2.0) and adopt the value of $\beta_o = -2.23$. We adopt the same intrinsic slope. In order to derive the $\kappa_{2300}/\kappa_{1500}$ ratio for different extinction curves, we convolve any given curve with the *GALEX* FUV and NUV filters. We find that, for a typical MW extinction curve, the additional absorption in the NUV band due to the 2200 Å absorption feature leads to even larger dust-corrected UV-based SFR estimates, making such relatively "flat" extinction curves unlikely. We then concentrate on "feature-free" and relatively steep extinction curves. The best known such extinction law is the one observed in the SMC (Prevot et al. 1984).[9] In Figure 9, we show the SMC extinction law, the Calzetti starburst extinction law (Calzetti 2001), and the MW $R_V = 3.1$ extinction law (Draine 2003) compared with the *GALEX* filters. We find that reconciling the global 24 μm SFR with the UV SFR requires an extinction law that lies in between the two curves. This can be described as a simple linear combination: $C_{\rm ext} = 0.81\ C_{\rm ext,Calzetti}{+}0.19\ C_{\rm ext,SMC}$ or $C_{\rm ext} = 0.61\ C_{\rm ext,MW}{+}0.39\ C_{\rm ext,SMC}$, where the latter largely reflects the influence of the 2000 Å feature. We can also compare this with the modified $A_{\rm FUV}$ relations found by Salim et al. (2007), who find that for their large sample of local UV-detected galaxies, the Meurer et al. (1999) relation (being specifically geared toward starbursts) generally overestimates $A_{\rm FUV}$. Using the Salim et al. (2007) relation, we find $A_{\rm FUV} = 1.42$, which would make the dust-corrected SFR(FUV) much more consistent with our best estimate of the true SFR.

We repeat this exercise on a region-by-region basis to potentially look for changes in the extinction curve across the galaxy. Table 2 shows the values for A_{1600} we derived following both Meurer et al. (1999) and Salim et al. (2007), as well the A_{1600} required to match the $\mathrm{SFR(24)_{H\,II}}$. We chose $\mathrm{SFR(24)_{H\,II}}$

[9] Here we made use of http://webast.ast.obs-mip.fr/hyperz/hyperz_manual1/node10.html.

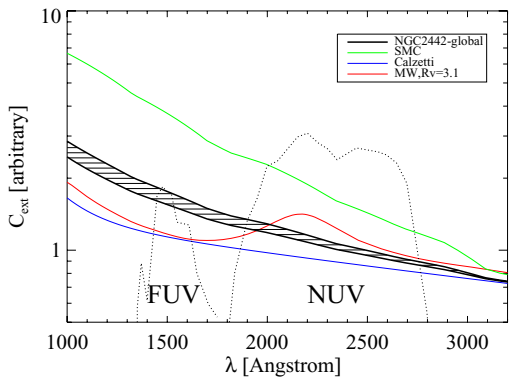

Figure 9. Extinction curve we need to reconcile the UV- and IR-based SFR estimates. Our estimates are found to lie between the SMC and Calzetti extinction laws and are defined as linear combinations of the two. The hashed region represents the range of 6–7 $M_{\odot}\mathrm{yr}^{-1}$ where the true SFR for NGC 2442 is most likely to lie.

(A color version of this figure is available in the online journal.)

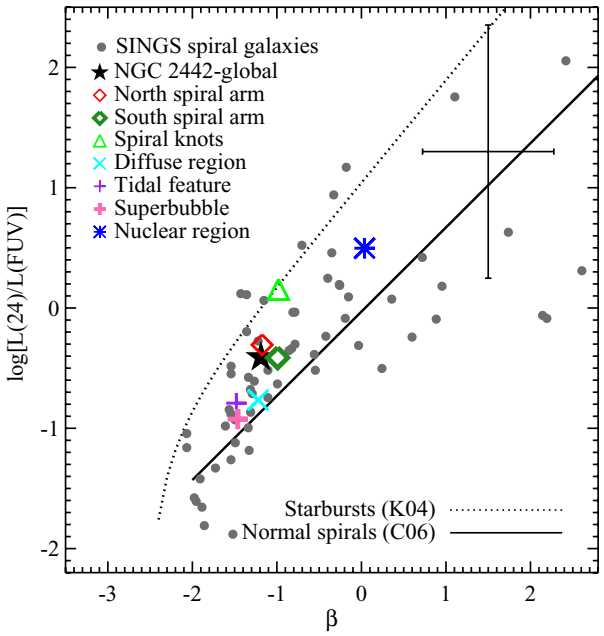

Figure 10. Modified IRX–β plot showing the average values for each region of interest as well as the total galaxy. The large error bar shows the typical spread in per-pixel values for each region. We also show relations for starbursts from Kong et al. (K04; 2004) and for normal spirals from Cortese et al. (C06; 2006). The gray filled circles show SINGS spiral galaxy data points from Dale et al. (2007).

(A color version of this figure is available in the online journal.)

as it gives the largest values (compared with $\mathrm{SFR}(24)_{\mathrm{global}}$ and SFR(FUV+24)) and therefore in most cases is closest to $\mathrm{SFR}(\mathrm{FUV})_{\mathrm{corr}}$. We discuss different choices below. We find that, as for the total galaxy, the Salim et al. (2007) relation for A_{1600} leads to closer agreement between SFR(FUV) and SFR(24) for most regions. Considering the typical scatter of the A_{1600} relation in Salim et al. (2007), we consider the match good for both spiral arms, as well as for the tidal and nuclear regions. Therefore, their extinction curves are probably not too dissimilar to that shown in Figure 9. The cases where there is significant deviation are the diffuse region, superbubble, and spiral knots. In both the cases of the diffuse region and the superbubble, the UV slope suggests far more reddening than needed to reconcile SFR(FUV) and SFR(24). In this case, choosing $\mathrm{SFR}(24)_{\mathrm{global}}$ leads to even worse agreement, and choosing SFR(FUV+24) makes little difference. Considering the full spread of the SFR(FUV) uncertainty (which is dominated by the systematic uncertainty on the IMF and star formation history), if we go to the upper limits of SFR(FUV) for these two regions, the discrepancy will be even larger. However, the lower limits on SFR(FUV) could bring the dust-corrected SFR(FUV) in agreement with SFR(24). As discussed previously, this may arise as a result of a significant, recent starburst (as can be seen in the Hα emission in the superbubble). A steeper extinction curve would also help reconcile the two SFR estimates. However, we find that, for example, to obtain the $A_{1600,\mathrm{IR-matched}}$ for the superbubble, we would need an unrealistic extinction curve that is much steeper than the SMC. The influence of recent starburst activity is much more likely. On the other hand, the spiral knots are the only region where the Meurer et al. (1999) relation for A_{1600} leads to better agreement between SFR(FUV) and SFR(24). Therefore, an extinction curve closer to the Calzetti (2001) starburst extinction is very likely. This is also not surprising given that this region has the strongest SFR intensity in this galaxy. The two are brought into even better alignment if the SFR(FUV+24) is considered instead of $\mathrm{SFR}(24)_{\mathrm{H\,II}}$.

4.6. The IRX–β Relation

The infrared-excess-β (IRX–β) relation compares $L(\mathrm{TIR})/L(\mathrm{FUV})$ and β, but since we do not have the total IR luminosity for the regions of interest in NGC 2442, we use $L(24)/L(\mathrm{FUV})$ and β. This modified IRX–β diagram is shown in Figure 10, showing the average for each region of interest, as well as for the total galaxy. We find slightly different averages for the regions of interest when we calculate $L(24)/L(\mathrm{FUV})$ and β using the total flux for each region versus when we calculate the per-pixel values and average them for each region. The representative error bar shown in Figure 10 is the 1σ spread in per-pixel values around the mean, not the error in the mean, which is much smaller given the large number of pixels in most regions. This plot also shows the relation for starbursts from Kong et al. (2004) and that for normal spirals from Cortese et al. (2006). To convert between $L(\mathrm{TIR})$ and $L(24)$, we use the method of Section 4.4.2 to compute the ratio of $L(\mathrm{TIR})/L(24)$. The $L(\mathrm{TIR})$ of Kong et al. (2004) is defined between 3 and 850 μm and we estimate $L(\mathrm{TIR})/L(24) \sim 11.37$. The $L(\mathrm{TIR})$ of Cortese et al. (2006) is defined between 1 and 1000 μm and we estimate a larger ratio of $L(\mathrm{TIR})/L(24) \sim 21.39$. The data for SINGS spiral galaxies from Dale et al. (2007) have been included to show the range of $L(24)/L(\mathrm{FUV})$ versus β values for a normal star-forming population. We find that our spiral knots alone are in good agreement with the starburst relation, while the rest of the regions and the total galaxy as a whole are in good agreement with the normal galaxies relation. Boquien et al. (2009b) argue that this spread between the normal star-forming galaxies and starbursts can be explained by differences in the extinction curve. Therefore, our spiral knots being closer to the starburst relation and likely having an extinction law comparable to Calzetti et al. (see the previous section) are consistent with this conclusion. However, we should keep in mind that in the previous section we assumed a constant β_o (i.e., dust-free UV slope). Variations in β_o, such as with higher contributions of older stars would affect this as well. However, with the inferred SFRs and intensities of this region, there should be plenty of young stars to dominate the UV emission.

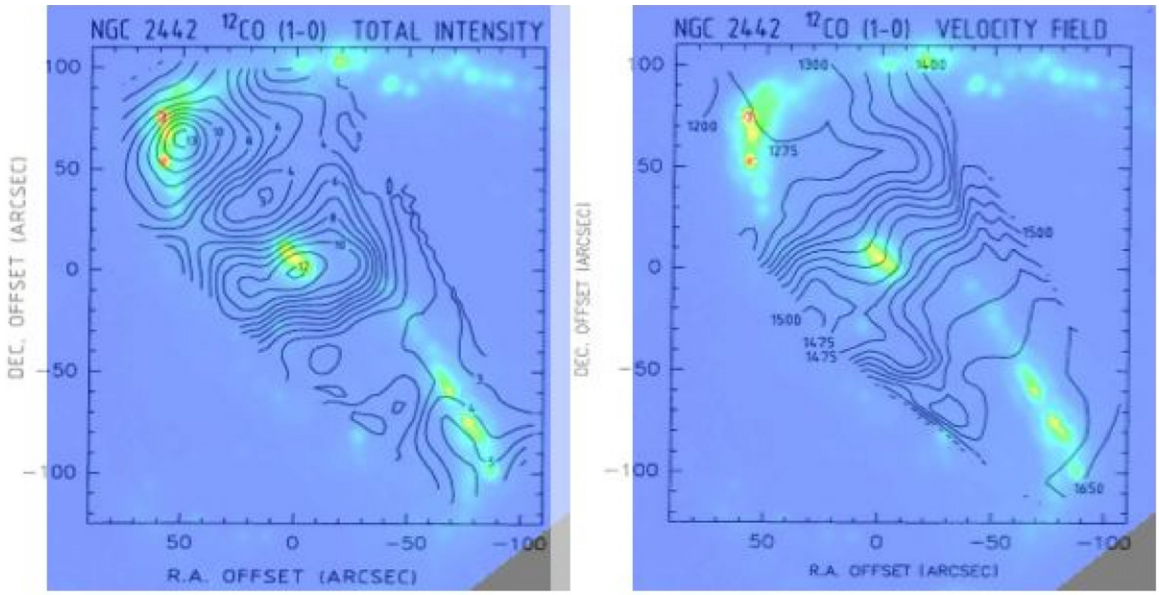

Figure 11. Here we overlay our MIPS 24 μm image (i.e., SFR) with the CO total intensity and velocity field images from Bajaja et al. (1995). The numbers in the right-hand panel correspond to the velocity contours in km s^{-1}. Note that the alignment between the background image and the contour images is done by eye and hence is only approximately correct. It is however clear that the strong SFR we observe in the northern arm is fueled by significant molecular gas. See Bajaja et al. (1995) for details on the CO observations. In this figure, north is up and east is left.

(A color version of this figure is available in the online journal.)

5. DISCUSSION

One of the principal questions we address in this paper is the global SFR and obscuration of NGC 2442. The only previous measurement of the SFR in NGC 2442 was presented in Ryder & Dopita (1994), who find 4.9 $M_{\odot}$yr^{-1} globally. This already has dust correction of $A_{0.65} = 0.45$ applied to it. The foreground extinction value is $A_{0.65} = 0.54$ (NED). Using the H_{α} luminosity as given in Mihos & Bothun 1997) and updating the luminosity distance and SFR relation (Kennicutt 1998), as well as the difference in foreground extinction values, we find SFR(Hα) = 4.6 $M_{\odot}$ yr^{-1}. Using UV, 8 μm, 24 μm, and composite (UV+24) estimates, we find values of 6–11 $M_{\odot}$yr^{-1} the latter being the UV-based estimate when corrected for dust using the Meurer relation. We conclude that the true SFR is most likely to lie in the range ~6–7 $M_{\odot}$yr^{-1} based on a wide range of relations including an H II region calibrated SFR(24) and integrated total galaxy light and TIR-calibrated SFR(24), as well as composite (Hα+24, Hα+TIR, and FUV+24) relations. This also agrees with the SFR(FUV) if we adopt the Salim et al. (2007) relations for both SFR(FUV) and $A_{\rm FUV}$. All of these relations are calibrated using nearby normal star-forming galaxies and are therefore applicable to NGC 2442.

This global agreement between the IR-based and UV-based SFR estimates for NGC 2442 requires a steeper UV extinction law—one in between the SMC and starburst (Calzetti) extinction curves, or between an MW-type and an SMC-type extinction. However, we do find that the areas of highest SFR intensity are consistent with the starburst extinction law, which may provide a hint for the range of applicability of different extinction laws. Recently, Siana et al. (2009) suggested that a steeper UV extinction might be required for at least some high redshift Lyman break galaxies as well, which highlights the need to understand this uncertainty better locally.

We find that the SFR in NGC 2442 most likely lies in the range ~6–7 $M_{\odot}$yr^{-1}, which is ~15%–35% higher than the value of SFR(Hα) alone. In order for the Hα emission to give the same value of SFR as the 24 μm it would have to be obscured by $A_{\rm H\alpha} \sim 0.3$–0.5 mag globally. The inferred UV obscuration value is $A_{1600} = 2.0$ (based on the Meurer relation) or $A_{1600} = 1.5$ (required to make the UV and 24 μm SFR estimates agree). Based on the Draine (2003) $R_V = 3.1$ MW extinction curve, we find $A_{6563}/A_{1600} = 0.30$, implying $A_{6563} = 0.4$–0.6. If we adopt the theoretical SMC extinction curve from Weingartner & Draine (2001), we find $A_{6563}/A_{1600} = 0.14$ implying $A_{6563} \sim 0.2$–0.3. An Hα extinction of $A_{\rm H\alpha} \sim 0.3$–0.5 required to reconcile our Hα SFR with our IR-based estimates is apparently in between these two values. However, if we consider differential attenuation between the stellar continuum and the ionized gas, we have $A_{\rm H\alpha} \sim 2.2\,A_{6563}$ (Calzetti 2001), implying that UV/optical extinction curve in NGC 2442 may be closer to the SMC after all. Note however that the uncertainties on all of these estimates are substantial and even more fundamentally that we have assumed a very simplistic geometry, in that everything is treated as a homogeneous dust screen.

Another aspect of this work was to address the spatial distribution of star formation and obscuration in NGC 2442 especially in light of its tidally distorted morphology. The IR emission (both 8 μm and 24 μm) is fairly clumpy and largely concentrated along the spiral arms, with the notable exception of the superbubble region. The UV emission does not correlate well with the IR emission in that there is relatively stronger FUV emission outside the spiral arms. The superbubble region and the tidal region at the tip of the southern arm are both particularly strong in the UV relative to the IR. We find that the highest SFR intensities are found in the 24 μm bright knots along the spiral arms, followed by the nuclear region which includes a circumnuclear ring. The nuclear region also has the highest levels of UV obscuration with $A_{1600} \sim 4$. The most unusual SEDs are observed for the superbubble region as well as the tidal region, which also has IRAC colors that deviate from the usual trend. The superbubble region, in particular, is believed to be an area of strong past and current star formation outside

of the spiral arms. We can also compare the Hα image from Mihos & Bothun (1997) with that of the other star formation tracers. Mihos & Bothun (1997) find that there is little diffuse Hα emission, with a majority concentrated in H II regions. The most luminous 24 μm and 8 μm regions tend to overlap with the H II regions (this can also be seen in Figure 5 for part of the galaxy). Figure 11 also shows a, by eye, comparison of the ^{12}CO (1–0) line intensity and velocity field as determined by Bajaja et al. (1995) with our MIPS 24 μm map of NGC 2442. Most clearly, the CO intensity exhibits two prominent peaks which correspond to the nucleus and the knots along the northern spiral arm. Both regions were identified above as having the highest SFR intensity. The star-forming knots along the southern spiral arm are somewhat weaker but do correspond to CO-bright regions as well. Our superbubble region also shows CO emission as expected for an active star-forming region.

Lastly, what does this mean in terms of the history of NGC 2442? It is still unclear whether NGC 2442 has undergone a tidal encounter with a neighboring galaxy or has suffered ram pressure stripping. A large cloud of hydrogen, a third the mass of NGC 2442's neutral gas, resides just north of the galaxy and may be a result of these violent processes (Ryder et al. 2001). Our best estimate for the total SFR in NGC 2442 (SFR $\sim$ 6–7 $M_{\odot}$yr^{-1}) is somewhat higher than typical in normal star-forming galaxies (see, e.g., Smith et al. 2007), suggesting enhanced star formation in addition to the morphological distortion (contrary to Mihos & Bothun 1997). The star formation is not overwhelmingly concentrated in the nuclear region, as expected in interacting galaxies (Smith et al. 2007), but is rather strong in clumps of intense star formation along the spiral arms. These regions in themselves display many properties of starburst galaxies including a strong PAH/stars ratio and potentially a more starburst-like extinction law. The northern spiral arm is stronger and much more pronounced than its southern counterpart and includes the clumps of highest SFR intensity, coincident with high molecular gas concentrations (Figure 11). In contrast, the southern part of the galaxy shows a weaker spiral arm which transitions into our "tidal region," as well as the superbubble region outside the spiral arm, which we associate with active star formation. This north–south asymmetry is rather convincingly explained by ram pressure stripping by Ryder et al. (2001) where the morphology and star formation strength of the northern arm are due to the bow shock where the galaxy plows into the IGM (see also Figure 11). The area of our superbubble region is a strong radio emitter (Harnett et al. 2004), in support of the role of supernovae in that region. While the above discussion generally supports the ram pressure stripping scenario, the details are not yet clear and further study is needed to truly explore the possibilities. In particular, we need to explore how common this type of galaxy might be at higher redshifts where we generally lack morphological information and where we expect typically denser environments. Detailed dynamical modeling of NGC 2442 would be especially useful for exploring NGC 2442's past and explaining the many interesting properties of this galaxy. The morphological and SED properties of the superbubble and tidal regions are unusual and unexpected on the basis of existing simulations of NGC 2442 (Mihos & Bothun 1997). Higher resolution radio observations of the superbubble region would help shed light on its nature (in particular, to see if the shell-like structure observed in the IRAC 8 μm image is visible there as well). A mid-IR spectrum of the tidal region would help us to better understand its peculiar IRAC colors.

Some caveats in our discussion need to be taken into account. While we were careful to use SFR relations that are applicable to our Galaxy and to characterize the associated uncertainties, ultimately our conclusions regarding the SFR globally and per region are *relative* to the original samples on which these relations were calibrated as well as any underlying assumptions (such as inherent in the Hα–SFR conversion). In addition, this galaxy has substantial foreground extinction (see Section 2.4). We correct for this prior to any subsequent analysis, but how would our conclusions be affected by uncertainties in the level of this foreground? Ultimately, our best estimates of the star formation in this galaxy arise from the infrared data and hence would be unchanged. The SFR(FUV) estimates are strongly affected by dust obscuration and hence, in practice, we use them primarily as a way to constrain the extinction curve in NGC 2442. Most simply put, a higher foreground would imply a more SMC-like extinction curve, while a lower foreground would imply a more MW-type dust. It is difficult to address this further, however, because of the large systematic uncertainties on SFR(FUV).

6. CONCLUSIONS

NGC 2442 is a nearby galaxy whose peculiar morphology is believed to arise either from tidal interaction with a neighboring galaxy or from ram pressure stripping which acts roughly south-to-north. The *GALEX* and *Spitzer* data allow us to explore the distribution and levels of star formation and dust obscuration in this galaxy. Our major regions of interest are the spiral arms, spiral knots of high 24 μm emission, nuclear region (including a circumnuclear ring), the diffuse region, a tidally distorted region at the southern tip of the galaxy, and a superbubble region inside the diffuse area. We employ various tracers of star formation: the FUV, 8 μm, and 24 μm emission as well as a composite FUV+24 SFR relation. For the total SFR, we also consider the H_{α} and total IR luminosities. The dust obscuration is traced using the UV–slope as well as by trying to reconcile the UV, H_{α}, and 24 μm based SFR estimates. We find the following.

1. Our best estimate for the total SFR of NGC 2442 is $\sim$6–7 $M_{\odot}$yr^{-1}. This is based on the 24 μm emission as well as a combination of FUV and 24 μm and Hα and total IR emission, as calibrated by Kennicutt et al. (2009).
2. The highest intensity star-forming regions are the spiral knots followed by the nuclear region. The nuclear region is the most obscured region of the galaxy. It also includes a $\sim$0.8 kpc radius circumnuclear ring that is especially prominent at 8 μm (i.e., PAH emission). The nuclear Hα emission shows a vague extended spiral structure that is largely contained inside this PAH ring.
3. A tidal debris region has unusual IRAC colors, which is consistent with similar findings from Smith et al. (2007). With only broadband data, we cannot say conclusively what is the cause for this, but it may be due to relatively higher levels of hot dust, or the presence of strong molecular or ionic emission lines, especially in the 5.8 μm band.
4. With standard UV–slope dust correction, the SFR(FUV) values are consistently higher than the IR-based estimates. We find that, globally, we can reconcile the FUV and 24 μm SFR estimates by a UV extinction law that is intermediate in slope between an SMC-like extinction and a Calzetti-like extinction. Regions of high star formation intensity, the spiral knots and the north spiral arm, are consistent

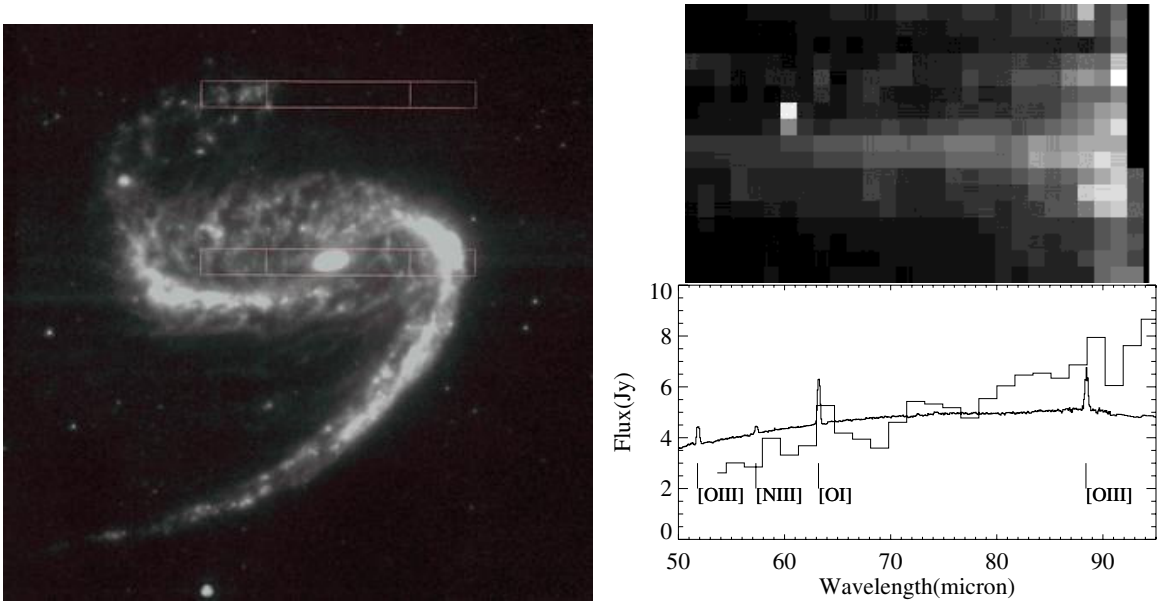

Figure 12. Left: the footprint of the MIPS SED observation overlaid on the IRAC 8 μm image. Right: two-dimensional and one-dimensional low-resolution MIPS SED-mode spectrum of the nuclear region of NGC 2442. For comparison, we also show the *ISO* spectrum of M82 (Colbert et al. 1999). Two features to note are that the NGC 2442 nuclear spectrum is fairly steeply rising and that it seems to contain a strong oxygen 63 μm line. Note however that the oxygen line is offset from the continuum by roughly ∼6″–15″. This suggests that while the observed continuum is likely associated with the nucleus itself, the oxygen line is more likely associated with the star-forming nuclear ring.

with the starburst-calibrated Calzetti extinction. A similar analysis to reconcile the Hα and UV-based SFRs suggests an optical/UV extinction slope intermediate between an MW-type and an SMC-type extinction.

5. We find what looks like a superbubble, ∼1.7 kpc across outside the spiral arms of NGC 2442. This structure is particularly prominent in the IRAC 8 μm image, although it can be seen in all of our IRAC images. After the spiral knots, the superbubble has the highest PAH-to-stars ratio, implying significant star formation. H_α and UV emission suggest significant star formation in the area as well. SN 1999ga is found at the edge of this structure.

We are grateful to the anonymous referee for their careful reading of our manuscript and thoughtful suggestions that have significantly improved the content and clarity of this paper. We thank Beth Willman and Brian Siana for helpful discussions. Support for this work was provided by NASA through an award issued by JPL/Caltech. This work is based in part on observations made with the *Spitzer Space Telescope*, which is operated by the Jet Propulsion Laboratory, California Institute of Technology under a contract with NASA. This work uses observations made by *Galaxy Evolution Explorer* (*GALEX*), a NASA Small Explorer, launched in 2003 April and developed in cooperation with the Centre National d'Etudes Spatiales of France and the Korean Ministry of Science and Technology. This work makes use of data products from the Two Micron All Sky Survey, which is a joint project of the University of Massachusetts and the Infrared Processing and Analysis Center/California Institute of Technology, funded by the National Aeronautics and Space Administration and the National Science Foundation. This work has also made use of the NASA/IPAC Extragalactic Database (NED) which is operated by the Jet Propulsion Laboratory, California Institute of Technology, under contract with the National Aeronautics and Space Administration.

APPENDIX

FURTHER DETAILS ON THE NUCLEAR REGION

As mentioned in the introduction, the nucleus of NGC 2442 is a LINER. The optical spectra (Bajaja et al. 1999) covering from ∼3500 to 7000 Å show some of the classical emission lines including: Hα, Hβ, [O II] 3727, [O III] 4959+5007, [N II]5755+6548+6584, [O I] 6300 (surprisingly not 6363), and [S II] 6717+6731. The fact that there is a significant energy source exciting the gas can be seen in that, for example, the optical [O III] 5007 is as bright as Hβ.

Although, we found that the nuclear IRAC colors were not in themselves indicative of an AGN, this is actually not surprising for LINERS. For example, FRI radio galaxies often show no IR emission from their AGN (Ogle et al. 2006). There is an on-off MIPS SED observation of the nuclear region of NGC 2442. This observation was made on 2004 February 20 (on the same day as the IRAC Chan4 image). The MIPS–SED FOV is ∼2.′7 × 0.′34 which covers the whole nuclear region (including the 8 μm ring), but it is also slightly contaminated by the edge of the spiral arm (see Figure 12, left). In Figure 12 (right), we show both the two-dimensional and one-dimensional MIPS SED, which is compared with the well-known spectrum of M82. The [O I] 63 μm line that we can see in the low-resolution SED spectrum appears to be offset from the nucleus itself as can be seen in the two-dimensional spectrum. It appears that the continuum likely originates in the nucleus itself whereas the oxygen emission is more likely associated with the ring. It is interesting that the continuum is rising compared with M82, which is rather "warm" for a starburst. As was already discussed in the context of the nucleus IRAC colors, this also suggests the lack of a hot AGN-heated torus.

The other interesting feature in the nuclear region is that in the IRAC images (especially at 8 μm) it can be separated into a compact nucleus and a ring of a radius of ∼0.8 kpc. In Figure 13, we compare the 8 μm emission (contours) with an archival ACS Hα image available through the MAST *HST*

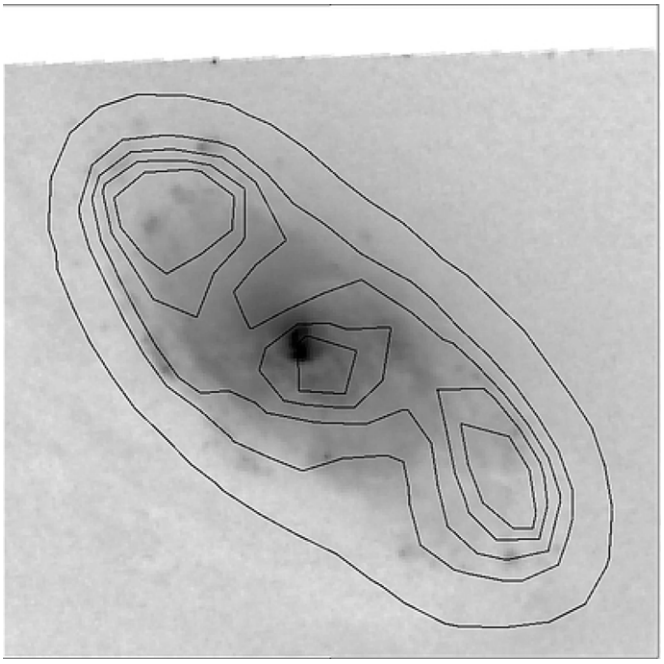

Figure 13. Here the gray scale shows the archival ACS Hα image with the IRAC 8 μm contours overlaid. The box is 20″ × 20″. North is up and east is left.

archive. The conclusions that can be drawn from this comparison are: (1) the Hα emission is largely inside the 8 μm ring meaning the latter can be interpreted as a higher obscuration/dustier region whose PAHs are excited by the stars inside the ring; (2) the Hα and 8 μm nuclei are slightly offset from each other, which could be due to obscuration, although some pointing offset cannot be excluded; and (3) the Hα nucleus is slightly resolved and there is a suggestion of spiral structure in the Hα image which type of structure has been seen in other star-forming galaxies; this supports the view that although an AGN is likely present (accounting for the LINER spectrum), significant nuclear star formation is also present. The strong (and rising) far-IR continuum seen in Figure 12 (right) also supports this view.

REFERENCES

Alonso-Herrero, A., Rieke, G. H., Rieke, M. J., Colina, L., Pérez-González, P. G., & Ryder, S. D. 2006, ApJ, 650, 835
Arp, H. 1966, ApJS, 14, 1
Bajaja, E., Agüero, E., & Paolantonio, S. 1999, A&AS, 136, 179
Bajaja, E., Wielebinski, R., Reuter, H.-P., Harnett, J. I., & Hummel, E. 1995, A&AS, 114, 147
Bigiel, F., Leroy, A., Walter, F., Brinks, E., de Blok, W. J. G., Madore, B., & Thornley, M. D. 2008, AJ, 136, 2846
Boquien, M., et al. 2009a, AJ, 137, 4561
Boquien, M., et al. 2009b, ApJ, 706, 553
Bridge, C. R., et al. 2007, ApJ, 659, 931
Buat, V., et al. 2005, ApJ, 619, L51
Calzetti, D. 2001, PASP, 113, 1449
Calzetti, D., Kinney, A. L., & Storchi-Bergmann, T. 1994, ApJ, 429, 582
Calzetti, D., et al. 2005, ApJ, 633, 871
Calzetti, D., et al. 2007, ApJ, 666, 870
Calzetti, D., et al. 2010, ApJ, 714, 1256
Chabrier, G. 2003, PASP, 115, 763
Charmandaris, V., Le Floc'h, E., & Mirabel, I. F. 2004, ApJ, 600, L15
Cohen, M., Wheaton, W. A., & Megeath, S. T. 2003, AJ, 126, 1090
Colbert, J. W., et al. 1999, ApJ, 511, 721
Cortese, L., et al. 2006, ApJ, 637, 242
Dale, D. A., et al. 2007, ApJ, 655, 863
Draine, B. T. 2003, ARA&A, 41, 241
Eskridge, P. B., et al. 2002, ApJS, 143, 73
Fazio, G. G., et al. 2004, ApJS, 154, 10
Gil de Paz, A., et al. 2007, ApJS, 173, 185
Harnett, J., Ehle, M., Fletcher, A., Beck, R., Haynes, R., Ryder, S., Thierbach, M., & Wielebinski, R. 2004, A&A, 421, 571
Jarrett, T. H., Chester, T., Cutri, R., Schneider, S. E., & Huchra, J. P. 2003, AJ, 125, 525
Kennicutt, R. C., Jr. 1998, ARA&A, 36, 189
Kennicutt, R. C., et al. 2009, ApJ, 703, 1672
Kong, X., Charlot, S., Brinchmann, J., & Fall, S. M. 2004, MNRAS, 349, 769
Le Floc'h, E., et al. 2005, ApJ, 632, 169
Lu, N., et al. 2003, ApJ, 588, 199
Maraston, C. 2005, MNRAS, 362, 799
Martin, D. C., et al. 2005, ApJ, 619, L1
Meurer, G. R., Heckman, T. M., & Calzetti, D. 1999, ApJ, 521, 64
Mihos, J. C., & Bothun, G. D. 1997, ApJ, 481, 741
Morrissey, P., et al. 2007, ApJS, 173, 682
Ogle, P., Whysong, D., & Antonucci, R. 2006, ApJ, 647, 161
Pastorello, A., et al. 2009, A&A, 500, 1013
Peeters, E., Hony, S., Van Kerckhoven, C., Tielens, A. G. G. M., Allamandola, L. J., Hudgins, D. M., & Bauschlicher, C. W. 2002, A&A, 390, 1089
Polletta, M., et al. 2007, ApJ, 663, 81
Prevot, M. L., Lequeux, J., Prevot, L., Maurice, E., & Rocca-Volmerange, B. 1984, A&A, 132, 389
Reddy, N. A., Steidel, C. C., Fadda, D., Yan, L., Pettini, M., Shapley, A. E., Erb, D. K., & Adelberger, K. L. 2006, ApJ, 644, 792
Relaño, M., Lisenfeld, U., Pérez-González, P. G., Vílchez, J. M., & Battaner, E. 2007, ApJ, 667, L141
Rieke, G. H., Alonso-Herrero, A., Weiner, B. J., Pérez-González, P. G., Blaylock, M., Donley, J. L., & Marcillac, D. 2009, ApJ, 692, 556
Rieke, G. H., et al. 2004, ApJS, 154, 25
Ryder, S. D., & Dopita, M. A. 1994, ApJ, 430, 142
Ryder, S. D., et al. 2001, ApJ, 555, 232
Sajina, A., Lacy, M., & Scott, D. 2005, ApJ, 621, 256
Salim, S., et al. 2007, ApJS, 173, 267
Salpeter, E. E. 1955, ApJ, 121, 161
Sersic, J. L., & Donzelli, C. 1993, A&AS, 98, 21
Shi, Y., Rieke, G., Lotz, J., & Perez-Gonzalez, P. G. 2009, ApJ, 697, 1764
Siana, B., et al. 2009, ApJ, 698, 1273
Skrutskie, M. F., et al. 2006, AJ, 131, 1163
Smith, B. J., Struck, C., Hancock, M., Appleton, P. N., Charmandaris, V., & Reach, W. T. 2007, AJ, 133, 791
Spergel, D. N., et al. 2003, ApJS, 148, 175
Tsai, A.-L., et al. 2009, PASJ, 61, 237
Vader, J. P., & Chaboyer, B. 1995, ApJ, 445, 691
Weingartner, J. C., & Draine, B. T. 2001, ApJ, 548, 296
Werner, M. W., et al. 2004, ApJS, 154, 1
Woodings, S., Martin, R., Williams, A., Biggs, J., & Verveer, A. 1999, IAU Circ., 7316, 1
Wu, H., Cao, C., Hao, C.-N., Liu, F.-S., Wang, J.-L., Xia, X.-Y., Deng, Z.-G., & Young, C. K.-S. 2005, ApJ, 632, L79
Zhang, H.-X., Gao, Y., & Kong, X. 2010, MNRAS, 401, 1839
Zhu, Y.-N., Wu, H., Cao, C., & Li, H.-N. 2008, ApJ, 686, 155